Cent. Eur. J. Phys. • 12(1) • 2014 • 42-56
DOI: 10.2478/s11534-014-0426-2

VERSITA

Central European Journal of **Physics**

# Superdeformed structures and low Ω parity doublet in Ne–S nuclei near neutron drip-line

**Research Article**

Shailesh K. Singh,* Choudhury R. Praharaj, Suresh K. Patra

*Institute Of Physics,*
*Bhubaneswar - 05, India*

**Received 25 September 2013; accepted 29 November 2013**

**Abstract:** The structures of Ne, Na, Mg, Al, Si, P and S nuclei near the neutron drip-line region are investigated in the frame-work of relativistic mean field theory and non-relativistic Skyrme Hartree-Fock formalism. The recently discovered nuclei $^{40}$Mg and $^{42}$Al, which are beyond the drip-line predicted by various mass formulae are located within these models. We find many largely deformed neutron-rich nuclei, whose structures are analyzed. From the structure anatomy, we find that at large deformation low Ω orbits of opposite parities (e.g. $\frac{1}{2}^+$ and $\frac{1}{2}^-$) occur close to each other in energy.

**PACS (2008):** 21.10.Dr, 21.10.Ft, 21.10.Hw, 21.10.Pc

**Keywords:** relativistic mean field theory • Skyrme Hartree-Fock theory • superdeformed shape • parity doublet • shape coexistence



## 1. Introduction

The structure of light nuclei near the neutron drip-line is an interesting topic for a good number of exotic phenomena. Nuclei in this region are quite different in collectivity and clustering features than their stable counterpart in the nuclear chart. For example, the neutron magic property is lost for N = 8 in $^{12}$Be [1–3] and N = 20 in $^{32}$Mg [4]. The unexpectedly large reaction cross-section for $^{22}$C gives an indication of neutron halo structure [5]. The discovery of large collectivity of $^{34}$Mg by Iwasaki et al. [6] is another example of such exotic properties. The deformed structures, core excitation, and the location of the drip-line for Mg and neighboring nuclei are a few of the interesting properties for investigation. In this context, the discovery of $^{40}$Mg and $^{42}$Al, once predicted to be nuclei beyond the drip-line by various mass formulae [7, 8], show the need for modification of the mass models.

On the other hand, the appearance of N = 16 as magic number in $^{24}$O and the existence of neutron halo in $^{11}$Li are established observations [9]. However, the proposed proton [10] ($^{8}$B) and neutron [11–13] halo ($^{14}$Be, $^{17}$B, $^{31}$Ne) in the exotic nuclei are currently under investigation. In addition to these, the cluster structure of the light mass nuclei and skin formation in neutron-drip isotopes motivate us to study of light mass drip-line nuclei. In this paper, our aim is to study the neutron drip-line for the Ne–S isotopic chain in the framework of the relativistic mean field (RMF) and nonrelativistic Skyrme Hartree-Fock (SHF) formalisms and analyze the features of large

*E-mail: shailesh@iopb.res.in

quadrupole deformation of these isotopes.

The paper is organized as follows: The RMF and SHF formalisms are described briefly in Section II. The results obtained from our calculations are discussed in Section III. Finally, a summary and concluding remarks are given in Section IV.

## 2. The formalism

Mean field methods like SHF and RMF have been widely used in the study of binding energies, root mean square radii, quadrupole deformation, and other bulk properties of nuclei [14, 15]. In general, one can say that although older parametrizations of SHF and RMF have some limitations in predicting experimental observables, recent version are good enough to reproduce the bulk properties not only near the $\beta-$stability line but also far away from it. Here, we use these two successful models [14–30] to learn about the properties of drip-line nuclei Ne–S.

### 2.1. The Skyrme Hartree-Fock (SHF) method

The general form of the Skyrme effective interaction used in the mean-field model can be expressed as a Hamiltonian density $\mathcal{H}$ [16–22]. This $\mathcal{H}$ is written expressed as a function of some empirical parameters given as:

$$\mathcal{H} = \mathcal{K} + \mathcal{H}_0 + \mathcal{H}_3 + \mathcal{H}_{eff} + \cdots , \tag{1}$$

where $\mathcal{K}$ is the kinetic energy term, $\mathcal{H}_0$ the zero range, $\mathcal{H}_3$ the density dependent, and $\mathcal{H}_{eff}$ the effective-mass dependent terms, which are relevant for calculating the properties of nuclear matter. These are functions of 9 parameters $t_i$, $x_i$ $(i = 0, 1, 2, 3)$ and $\eta$, and are given as

$$\mathcal{H}_0 = \frac{1}{4}t_0\left[(2+x_0)\rho^2 - (2x_0+1)(\rho_p^2+\rho_n^2)\right], \tag{2}$$

$$\mathcal{H}_3 = \frac{1}{24}t_3\rho^\eta\left[(2+x_3)\rho^2 - (2x_3+1)(\rho_p^2+\rho_n^2)\right], \tag{3}$$

$$\mathcal{H}_{eff} = \frac{1}{8}\left[t_1(2+x_1)+t_2(2+x_2)\right]\tau\rho + \frac{1}{8}\left[t_2(2x_2+1)-t_1(2x_1+1)\right](\tau_p\rho_p+\tau_n\rho_n) \tag{4}$$

The kinetic energy $\mathcal{K} = \frac{\hbar^2}{2M}\tau$, a form used in the Fermi gas model for non-interacting Fermions. The other terms, representing the surface contributions of a finite nucleus with $b_4$ and $b_4'$ as additional parameters, are

$$\mathcal{H}_{S\rho} = \frac{1}{16}\left[3t_1(1+\frac{1}{2}x_1) - t_2(1+\frac{1}{2}x_2)\right](\vec{\nabla}\rho)^2 - \frac{1}{16}\left[3t_1(x_1+\frac{1}{2}) + t_2(x_2+\frac{1}{2})\right] \times \left[(\vec{\nabla}\rho_n)^2 + (\vec{\nabla}\rho_p)^2\right], \tag{5}$$

$$\mathcal{H}_{S\vec{J}} = -\frac{1}{2}\left[b_4\rho\vec{\nabla}\cdot\vec{J} + b_4'(\rho_n\vec{\nabla}\cdot\vec{J_n} + \rho_p\vec{\nabla}\cdot\vec{J_p})\right]. \tag{6}$$

Here, the total nucleon number density $\rho = \rho_n + \rho_p$, the kinetic energy density $\tau = \tau_n + \tau_p$, and the spin-orbit density $\vec{J} = \vec{J_n} + \vec{J_p}$. The subscripts $n$ and $p$ refer to neutron and proton, respectively. The nucleon mass is represented by $m$. $\vec{J_q} = 0$, $q = n$ or $p$, for spin-saturated nuclei, i.e., for nuclei with major oscillator shells completely filled or empty. The total binding energy (BE) of a nucleus is the integral of $\mathcal{H}$.

### 2.2. The relativistic mean field (RMF) method

The relativistic mean field approach is well-known and the theory is well documented [23–28]. Here we start with the relativistic Lagrangian density for a nucleon-meson many-body system as:

$$\mathcal{L} = \overline{\psi_i}\{i\gamma^\mu\partial_\mu - M\}\psi_i + \frac{1}{2}\partial^\mu\sigma\partial_\mu\sigma - \frac{1}{2}m_\sigma^2\sigma^2 - \frac{1}{3}g_2\sigma^3 - \frac{1}{4}g_3\sigma^4 - g_s\overline{\psi_i}\psi_i\sigma - \frac{1}{4}\Omega^{\mu\nu}\Omega_{\mu\nu} + \frac{1}{2}m_w^2V^\mu V_\mu - g_w\overline{\psi}_i\gamma^\mu\psi_iV_\mu - \frac{1}{4}\vec{B}^{\mu\nu}.\vec{B}_{\mu\nu} + \frac{1}{2}m_\rho^2\vec{R}^\mu.\vec{R}_\mu - g_\rho\overline{\psi}_i\gamma^\mu\vec{\tau}\psi_i.\vec{R}^\mu - \frac{1}{4}F^{\mu\nu}F_{\mu\nu} - e\overline{\psi}_i\gamma^\mu\frac{(1-\tau_{3i})}{2}\psi_iA_\mu. \tag{7}$$

All the quantities have their usual meanings. From the relativistic Lagrangian, we obtain the field equations for the nucleons and mesons. These equations are solved by expanding the upper and lower components of the Dirac spinor and the boson fields in an axially deformed harmonic oscillator basis. The set of coupled equations is solved numerically by a self-consistent iteration method. The total energy of the system in RMF formalism is given by

$$E_{total} = E_{part} + E_\sigma + E_\omega + E_\rho + E_c + E_{pair} + E_{c.m.}, \tag{8}$$

where $E_{part}$ is the sum of the single particle energies of the nucleons and $E_\sigma$, $E_\omega$, $E_\rho$, $E_c$, $E_{pair}$, $E_{cm}$ are the contributions of the meson fields, the Coulomb field, pairing energy, and the center-of-mass energy, respectively.

## 2.3. Pairing correlation

To take care of the pairing correlation for open shell nuclei, the constant gap BCS-approach is used in our calculations. The pairing energy expression is written as:

$$E_{pair} = -G\left[\sum_{i>0} u_i v_i\right]^2, \tag{9}$$

with $G$=pairing force constant, and $v_i^2$ and $u_i^2 = 1 - v_i^2$ are the occupation probabilities[31, 32]. The variational approach with respect to $v_i^2$ gives the BCS equation [31]

$$2\epsilon_i u_i v_i - \triangle(u_i^2 - v_i^2) = 0, \tag{10}$$

using $\triangle = G\sum_{i>0} u_i v_i$. The occupation number is defined as:

$$n_i = v_i^2 = \frac{1}{2}\left[1 - \frac{\epsilon_i - \lambda}{\sqrt{(\epsilon_i - \lambda)^2 + \triangle^2}}\right]. \tag{11}$$

The chemical potentials $\lambda_n$ and $\lambda_p$ are determined by the particle numbers for neutrons and protons. The pairing energy is computed as $E_{pair} = -\triangle\sum_{i>0} u_i v_i$. For a particular value of $\triangle$ and $G$, the pairing energy $E_{pair}$ diverges, if it is extended to an infinite configuration space. In fact, in all realistic calculations with finite range forces, the contribution of states of large momenta above the Fermi surface (for a particular nucleus) to $\triangle$ decreases with energy. We use a pairing window, where the equations are extended up to the level $|\epsilon_i - \lambda| \leq 2(41A^{-1/3})$. The factor of 2 has been determined so as to reproduce the pairing correlation energy for neutrons in $^{118}$Sn using Gogny force [23, 32, 33]. The values of $\triangle_n$ and $\triangle_p$ are taken from [34], as input in the BCS-equation.

We compare the results with various simple and sophisticated pairing prescriptions like BCS-delta force [35] and BCS density dependent delta force [36]. These calculations have been done only for $^{20}$Ne and $^{47}$Al nuclei in both SkI4 and NL3 force parameter sets. We have given these results in Table 1 along with experimental results such as quadrupole deformation parameter $\beta_2$ [37], total binding energy (BE) [38], and root mean square charge radius ($r_{ch}$) [39]. We find that, for this lighter mass region of the periodic chart, pairing is less important for the majority of cases. With pairing, the deformation becomes negligible for $^{20}$Ne and we do not get the experimental deformation parameter in RMF calculations. With no pairing, we reproduce substantially the deformation parameter in RMF because the *density of states* near the Fermi surface for such light nuclei are small and not conducive to pairing [40, 41]. To understand the influence of pairing on open shell nuclei, we have taken into account the experimental data, wherever available. The SHF(SkI4) results are used as guidelines in the absence of these data. We realized after comparing the calculated $\beta_2$ from RMF and SHF with experimental data that the quadrupole deformation of SHF is closer to experiment without taking pairing correlation into account. For example, when we use the $\triangle_n$ and $\triangle_p$ from the experimental binding energy of odd-even values or from the empirical formula of Ref. [34, 42] to calculate $\beta_2$ for $^{20,22,24,26,28}$Ne in RMF(NL3), we find $\beta_2 \sim 0.18, 0.35, 0.19, 0.0, 0.0$, respectively, for these isotopes, agreeing with the result of Lalazissis et al [43]. These $\beta_2$ strongly disagree with the measured values ($\beta_2(expt.) = 0.723, 0.562, 0.45, 0.498, 0.50$) [37]. Similar effects are also seen in other considered isotopes. On the other hand, if we ignore pairing, then the calculated results are often better and these $\beta_2$ are quite close to the experimental data. The influence of pairing is also visible in the total binding energy. In some of the cases, even a couple of MeV difference in total binding energy is found with and without taking pairing correlation into account in RMF formalism. Contrary to the RMF, the pairing in the SHF formalism is almost insensitive to quadrupole deformation for the considered mass region. Thus, we have performed the calculations through out the paper without consideration of pairing.

## 2.4. Pauli blocking and harmonic oscillator basis

For even-even nucleus the $\pm m$ orbits are pairwise occupied and the mean field has time reversal symmetry. But in the case of an odd nucleon the time reversal symmetry is broken. To take care of the odd nucleon, we employ the blocking method [44]. We put the last nucleon in one of the conjugate states ±m and keep the other state empty. In this way we follow the time reversal symmetry for odd-even and odd-odd nuclei. We repeat this calculation by putting the odd nucleon in all of the nearby states of the conjugate level to determine the maximum binding energy of the ground state [44, 45].

In our present calculations the nuclei are treated as axial-symmetrically deformed, with the $z$-axis as the symmetry axis. Spherical symmetry is no longer present in general and therefore $j$ is not a good quantum number any more. Because of axial symmetry, each orbit is denoted by the quantum number $m$ of $J_z$ and is a superposition of $|jm>$ states with various $j$ values. The densities are invariant with respect to a rotation around the symmetry axis. For numerical calculations, the wavefunctions are expanded in a deformed harmonic oscillator potential basis and solved self-consistently in an iteration method.

**Table 1.** Calculation of binding energy (BE), quadrupole deformation parameter $\beta_2$, root mean square of matter radius ($r_{rms}$) and charge radius ($r_{ch}$) by taking various pairing methods. We have given these results for both SkI4 and NL3 parameter sets with experimental data [37–39].

| SkI4 | | | | | |
|---|---|---|---|---|---|
| Nucleus | Type of Pairing | $\beta_2$ | $r_{rms}$ | $BE$ | $r_{ch}$ |
| $^{20}$Ne | No pairing | 0.549 | 2.911 | 156.8 | 3.030 |
| | BCS-delta force | 0.548 | 2.910 | 156.8 | 3.030 |
| | BCS-dens.dep.delta-force | 0.548 | 2.910 | 156.8 | 3.030 |
| $^{47}$Al | No pairing | 0.006 | 3.972 | 287.8 | 3.324 |
| | BCS-delta force | 0.007 | 3.957 | 288.7 | 3.317 |
| | BCS-dens.dep.delta-force | 0.055 | 3.970 | 288.0 | 3.322 |
| NL3 | | | | | |
| $^{20}$Ne | No pairing | 0.537 | 2.846 | 156.7 | 2.972 |
| | BCS-delta | 0.036 | 2.920 | 154.9 | 3.055 |
| $^{47}$Al | No pairing | 0.090 | 3.832 | 294.6 | 3.246 |
| | BCS-delta | 0.081 | 3.834 | 294.8 | 3.246 |
| Exp. Results [37–39] | | | | | |
| $^{20}$Ne | | 0.728 | | 160.6 | 3.005 |
| $^{47}$Al | | | | — | |

The major oscillator quanta for Fermion $N_F$ and bosons $N_B$ are taken as $N_{max} = 12$. The convergence of our numerical results is tested in Fig. 1 for BE, matter radius $r_{rms}$, and quadrupole deformation parameter for some selected nuclei like $^{48}$Al, $^{49}$Si, and $^{56}$S. Here, the results are estimated from $N_F = N_B = 8$ to $N_F = N_B = 18$, and are shown in Fig. 1. From this analysis, we observed that the $\beta_2$ values are almost identical with the variation of oscillator quanta. However, the rms radii and binding energy vary until $N_F = N_B = 12$, beyond which the results are unchanged. It is well known that a harmonic oscillator basis is not suitable in dripline nuclei due to the asymptotic behavior of the density distribution. To resolve this problem, efforts have been made for solving the equations in coordinate space [46–48]. Some other kinds of bases like the transformed harmonic oscillator basis [49], the Gaussian expansion method [50], and the Woods-Saxon basis [51, 52] are also available in literature. The inclusion of a sufficiently large harmonic oscillator model space gives reasonably convergent results. This type of prescription is already done in Ref. [53]. However, to include continuum effects fully more work has to be done (by use of basis of finite potentials and inclusion of correlation effects in a Hartree-Bogoliubov scheme [54]).

## 2.5. Ground state properties from the SHF and RMF models

Certainly, for light mass nuclei the correction of centre of mass motion can not be ignored and it should be done self-consistently. That means, in the evaluation of centre-of-mass energy, one should evaluate $E_{CM} = \frac{<F|P^2|F>}{2M}$ using $|F>= |F>_{RMF}$ wavefunction. In this case, one has to calculate the matrix elements directly. However, this procedure is more involved and in the present calculations we have subtracted the spurious centre-of-mass motion using the Elliott-Skyrme approximation, where the approximate analytical expression is written as $E_{CM} = \frac{3}{4}.41A^{-1/3}$ MeV (harmonic oscillator approximation) with A is the mass number [55–57], and expect that the two results should not differ drastically. The quadrupole moment deformation parameter $\beta_2$ is evaluated from the resulting proton and neutron quadrupole moments through:

$$Q = Q_n + Q_p = \sqrt{\frac{16\pi}{5}} \left( \frac{3}{4\pi} AR^2 \beta_2 \right), \qquad (12)$$

where R = $1.2A^{1/3}$. The root mean square radii of protons and matter distribution are defined as $\langle r_p^2 \rangle = \frac{1}{Z} \int \rho_p(r_\perp, z) r^2 d\tau$, and $\langle r_{rms}^2 \rangle = \frac{1}{A} \int \rho(r_\perp, z) r^2 d\tau$, respectively, where $Z$ is the proton number and $\rho_p(r_\perp, z)$ is the deformed proton and $\rho(r_\perp, z)$ is the total nucleon density distribution. The proton and charge rms radius is connected through the relation $r_{ch} = \sqrt{r_p^2 + 0.64}$ [45].

We use the well known NL3 parameter set [58] for the RMF formalism. This set not only reproduces the properties of stable nuclei but also predicts well for those far from the $\beta$-stability valley. Also, the isoscalar monopole energy agrees excellently with the experimental values for different regions of the Periodic Table. The measured superdeformed minimum in $^{194}$Hg is 6.02 MeV above the ground state, whereas in the RMF calculation with NL3 set, this number is 5.99 MeV [58].

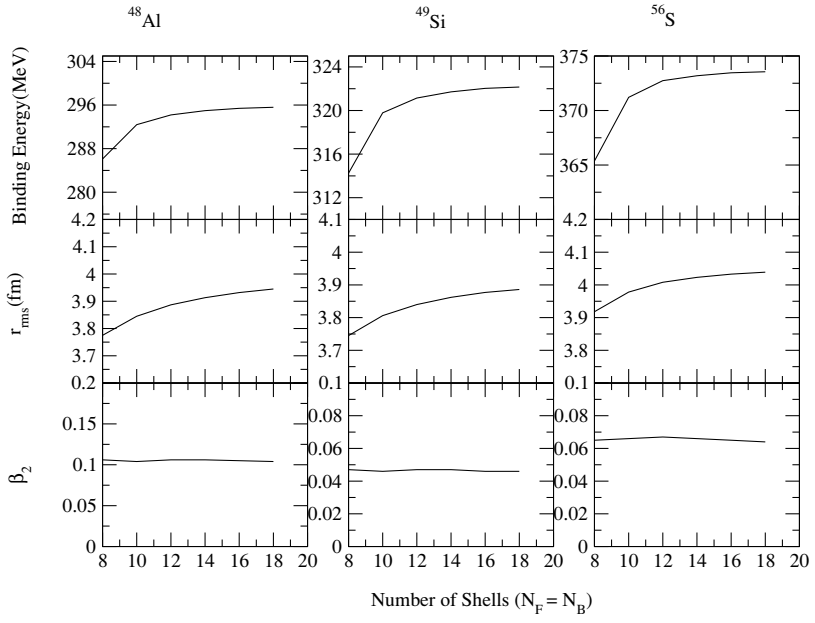


**Figure 1.** The change in binding energy BE, root mean square matter radius ($r_{rms}$), and quadrupole deformation parameter $\beta_2$ with Fermionic $N_F$ and bosonic $N_B$ harmonic oscillator basis for some selected nuclei.

For the SHF model, we use the Skyrme SkI4 set with $b_4 \neq b'_4$ [29]. This parameter set is designed for considerations of proper spin-orbit interaction in finite nuclei, related to the isotope shifts in the Pb region, and is better suited for the study of exotic nuclei. Several more recent Skyrme parameters such as SLy1-10, SkX, SkI5, and SkI6 are obtained by fitting the Hartree-Fock (HF) results with experimental data for nuclei starting from the valley of stability to neutron and proton drip-lines [16, 29, 30, 59].

**Table 2.** The calculated ground state binding energy obtained from the SHF and RMF theories are compared with the experimentally known heaviest isotope for Ne, Na, Mg, Al, Si, P and S [38].

| Nucleus | RMF | SHF | Expt. | Nucleus | RMF | SHF | Expt. |
|---|---|---|---|---|---|---|---|
| $^{31}$Ne | 216.0 | 213.2 | 211.4 | $^{32}$Na | 234.5 | 233.4 | 230.9 |
| $^{36}$Mg | 263.9 | 260.2 | 260.8 | $^{38}$Al | 283.5 | 281.4 | 280.3 |
| $^{41}$Si | 310.1 | 307.2 | 307.9 | $^{43}$P | 331.7 | 329.0 | 330.7 |
| $^{45}$S | 353.4 | 350.4 | 354.7 | | | | |

## 3. Results and discussions

The binding energy BE, rms charge radius $r_{ch}$, and quadrupole deformation parameter $\beta_2$ of the isotopes of Ne, Na, Mg, Al, Si, P, and S are calculated near the drip-line region. For this, both the relativistic and non-relativistic models are used.

### 3.1. Binding energy and neutron drip-line

The ground state binding energy (BE) for Ne, Na, Mg, Al, Si, P, and S isotopes are selected by comparing the binding energy obtained from the prolate, oblate, and spherical solutions for a particular nucleus. For a given nucleus, the maximum binding energy corresponds to the ground state and other solutions are obtained as various excited intrinsic states. In Table 2, the ground state binding energy for the heaviest known isotopes for the discussed nuclei are compared with the experimental data [38]. The binding energy for $^{31}$Ne is 216.0 MeV for RMF (NL3) and 213.2 and 211.4 MeV in SHF(SkI4) and experiment, respectively. Similarly, these results for $^{45}$S respectively are 353.4, 350.4, and 354.7 MeV for RMF, SHF, and experiment. Analyzing the data of Table 2, generally one finds that the BE of RMF is slightly overestimated and that in SHF is underestimated with respect to the experimental values. However, the overall agreement of the calculated energies are within an acceptable range with the experimental data.

We have listed the neutron drip-lines in Table 3, which

**Table 3.** The predicted mass number of neutron drip-line for Ne, Na, Mg, Al, Si, P and S nucleus in RMF (NL3) and SHF (SKI4) parameter sets are compared with infinite nuclear matter (INM) mass model [60], finite range droplet model (FRDM) [61] and the nuclei with the largest neutron numbers so far experimentally detected [38] along with experimentally extrapolated values shown in parentheses.

| Nucleus | RMF | SHF | INM | FRDM | Expt. |
|---|---|---|---|---|---|
| Ne | 34 | 34 | 34 | 33 | 31 (34) |
| Na | 40 | 37 | 37 | 36 | 32 (37) |
| Mg | 40 | 40 | 39 | 40 | 36 (40) |
| Al | 48 | 48 | 42 | 42 | 38 (43) |
| Si | 54 | 48 | 45 | 43 | 41 (45) |
| P | 54 | 55 | 49 | 48 | 43 (47) |
| S | 55 | 55 | 51 | 51 | 45 (49) |

are obtained from the ground state binding energy for neutron-rich Ne, Na, Mg, Al, Si, P, and S nuclei. The drip-line is determined by setting the condition that the minimum value of two-neutron separation energy $S_{2n} = BE(N,Z) - BE(N-2,Z) \geq 0$. The nuclei with the largest neutron numbers so far experimentally detected in an isotopic chain along with the extrapolated data are also displayed in the last column of Table 3. The numbers given in parentheses are the experimentally extrapolated values [38]. To get a qualitative understanding of the prediction of neutron drip-line, we have compared our results with the infinite nuclear matter (INM) [60] and finite range droplet model (FRDM) [61] mass estimations. The RMF and SHF drip-lines coincide with each other for Ne, Mg, Al, and S. In case of Na and Si the RMF drip nuclei are found to be 3 and 6 units heavier than the SHF prediction. The INM predictions for drip nuclei are always on the heavier side than those from FRDM. From Table 3, we find that the experimental effort has almost reached to the INM and FRDM prediction of drip nuclei for the lighter mass region.

The theoretical predictions of drip nuclei are very important after the discovery of $^{40}$Mg and $^{42}$Al [7]. These two nuclei are considered to be beyond the drip-line (neutron-unbound) in some of the mass calculations [8, 62]. The discovery of these two isotopes suggests the existence of a drip-line somewhere in the heavier side. Thus, the study of these isotopes is beyond the scope of the existing mass models [8, 62]. In the present RMF/SHF calculations, the newly discovered $^{40}$Mg and $^{42}$Al are well within the drip-line. Also, as a point of caution, it may be possible that if we allow triaxial deformation in the calculation then we may get one minimum as a saddle point and another one as a triaxial minimum. However, this calculation is out of the scope of our paper, as we are dealing with axial deformed code by using the NL3 and SkI4 parameter sets, where we mostly find similar results in both formalisms. These types of prescriptions are used in many of the earlier publications [63].

## 3.2. Neutron configuration

Analyzing the neutron configuration for these exotic nuclei, we notice that for lighter isotopes of Ne, Na, Mg, Al, Si, P, and S the oscillator shell $N_{osc} = 3$ is empty in the $[N_{osc}, n_3, \Lambda]\Omega^{\pi}$. However, the $N_{osc} = 3$ shell gets occupied gradually with increasing neutron number. In the case of Na, $N_{osc} = 3$ starts filling up at $^{33}$Na with quadrupole moment deformation parameters $\beta_2 = 0.356$ and $-0.179$ with occupied orbits $[330]\frac{1}{2}^-$ and $[303]\frac{7}{2}^-$, respectively. The filling of $N_{osc} = 3$ goes on increasing for Na with neutron number and it is $[330]\frac{1}{2}^-$, $[310]\frac{1}{2}^-$, $[321]\frac{3}{2}^-$, and $[312]\frac{5}{2}^-$ at $\beta_2 = 0.472$ for $^{39}$Na. Again for the oblate solution the occupation is $[301]\frac{1}{2}^-$, $[301]\frac{3}{2}^-$, $[303]\frac{5}{2}^-$, and $[303]\frac{7}{2}^-$ for $\beta_2 = -0.375$ for $^{39}$Na. In case of Mg isotopes, even for $^{30,32}$Mg the $N_{osc} = 3$ shell has some occupation for the low-lying excited states near the Fermi surface. For $^{30}$Mg (at $\beta_2 = 0.599$ with BE = 237.7 MeV), the $N_{osc} = 3$ orbit is $[330]\frac{7}{2}^-$ and for $^{32}$Mg it is $[330]\frac{1}{2}^-$ (BE = 248.8 MeV at $\beta_2 = 0.471$). With increasing of neutron number in Mg and Si isotopic chains, the oscillator shell with $N_{osc} = 3$ gets occupied more and more.

In Tables (4 – 6) the results for the ground state solutions are displayed. Thus, the prolate solutions have more binding than the oblate ones for Ne, Na, Mg, and S isotopes. In some cases, like $^{24-30}$Ne the prolate and oblate solutions are in degenerate states. For example, $^{24}$Ne has BE = 188.9 and 189.1 MeV at $\beta_2 = 0.278$ and $-0.259$ respectively. Contrary to this, the ground state solutions for Al and Si are mostly oblate. For example, $^{34}$Al has BE = 269.9 and 275.1 MeV at $\beta_2 = 0.159$ and $-0.108$ respectively. In such cases, the prolate solutions are in low-lying excited intrinsic states. Note that in many cases, there exist low-lying superdeformed states.

It is important to list some of the limitations of the results due to the input parameters, mostly coming from $E_{pair}$ and $E_{cm}$ energies. As one can see from Fig. 3, in many cases there are solutions of different shapes lying only a few MeV higher, sometimes even degenerate with the ground states. Such a few MeV difference is within the uncertainty of the predicted binding energies. A slight change in the pairing parameter, among other things, may alter the prediction for the ground state shape. With a few MeV uncertainty in ground state binding energies, by reassigning the ground state configurations the deformation may change completely, and make the predictions close to each other and agree with the FRDM predictions as well.

**Table 4.** The calculated values of charge radius ($r_{ch}$), quadrupole moment deformation parameter $\beta_2$, and binding energy (BE) for Ne, Na and Mg nuclei in RMF (NL3) and SHF (SkI4) formalisms. We compare our results with experimental $\beta_2$ [37], ground state binding energy BE (MeV) [38], and charge radius $r_{ch}(fm)$ [39].

| Nucleus | RMF (NL3) | | | SHF (SkI4) | | | Exp. | | |
|---|---|---|---|---|---|---|---|---|---|
| | $r_{ch}$ | $\beta_2$ | BE | $r_{ch}$ | $\beta_2$ | BE | $r_{ch}$ | $\beta_2$ | BE |
| $^{20}$Ne | 2.970 | 0.535 | 156.7 | 3.030 | 0.550 | 156.8 | 3.006 | 0.727 | 160.6 |
| $^{21}$Ne | 2.953 | 0.516 | 165.9 | 3.012 | 0.529 | 166.8 | 2.970 | | 167.4 |
| $^{22}$Ne | 2.940 | 0.502 | 175.7 | 3.010 | 0.520 | 175.8 | 2.953 | 0.562 | 177.8 |
| $^{23}$Ne | 2.913 | 0.386 | 181.8 | 2.975 | 0.382 | 182.2 | 2.910 | | 183.0 |
| $^{24}$Ne | 2.881 | -0.259 | 189.1 | 2.950 | -0.250 | 188.5 | 2.901 | 0.45 | 191.8 |
| $^{25}$Ne | 2.907 | 0.272 | 194.2 | 2.948 | 0.170 | 194.2 | 2.932 | | 196.0 |
| $^{26}$Ne | 2.926 | 0.277 | 199.9 | 2.950 | 0.120 | 199.4 | 2.925 | 0.498 | 201.6 |
| $^{27}$Ne | 2.945 | 0.247 | 203.9 | 2.987 | 0.159 | 203.2 | | | 203.1 |
| $^{28}$Ne | 2.965 | 0.225 | 208.2 | 3.010 | 0.160 | 206.5 | 2.964 | 0.50 | 206.9 |
| $^{29}$Ne | 2.981 | 0.161 | 211.2 | 3.027 | 0.010 | 210.1 | | | 207.8 |
| $^{30}$Ne | 2.998 | 0.100 | 215.0 | 3.050 | 0.000 | 213.7 | | | 211.3 |
| $^{31}$Ne | 3.031 | 0.244 | 216.0 | 3.057 | 0.225 | 213.2 | | | 211.4 |
| $^{32}$Ne | 3.071 | 0.373 | 218.6 | 3.100 | 0.380 | 213.1 | | | |
| $^{33}$Ne | 3.095 | 0.424 | 219.5 | 3.148 | 0.429 | 213.5 | | | |
| $^{34}$Ne | 3.119 | 0.473 | 220.9 | 3.180 | 0.490 | 213.5 | | | |
| $^{24}$Na | 2.964 | 0.379 | 192.3 | 3.042 | 0.411 | 194.0 | 2.974 | | 193.5 |
| $^{25}$Na | 2.937 | 0.273 | 200.6 | 3.024 | 0.314 | 201.4 | 2.977 | | 202.5 |
| $^{26}$Na | 2.965 | 0.295 | 207.1 | 3.027 | 0.274 | 208.4 | 2.993 | | 208.1 |
| $^{27}$Na | 2.993 | 0.323 | 214.2 | 3.043 | 0.282 | 214.9 | 3.014 | | 214.8 |
| $^{28}$Na | 2.993 | 0.272 | 219.0 | 3.058 | 0.234 | 219.7 | 3.040 | | 218.4 |
| $^{29}$Na | 3.004 | 0.232 | 224.3 | 3.072 | 0.194 | 224.3 | 3.092 | | 222.8 |
| $^{30}$Na | 3.031 | 0.169 | 228.1 | 3.079 | 0.030 | 228.6 | 3.118 | | 225.1 |
| $^{31}$Na | 3.047 | 0.108 | 232.7 | 3.103 | 0.000 | 233.5 | 3.170 | | 229.3 |
| $^{32}$Na | 3.077 | 0.237 | 234.5 | 3.121 | 0.187 | 233.4 | | | 230.9 |
| $^{33}$Na | 3.113 | 0.356 | 237.9 | 3.172 | 0.352 | 234.9 | | | |
| $^{34}$Na | 3.137 | 0.404 | 239.8 | 3.198 | 0.407 | 236.2 | | | |
| $^{35}$Na | 3.161 | 0.450 | 242.3 | 3.224 | 0.457 | 237.4 | | | |
| $^{36}$Na | 3.175 | 0.481 | 242.5 | 3.235 | 0.501 | 237.5 | | | |
| $^{37}$Na | 3.190 | 0.512 | 243.1 | 3.251 | 0.541 | 237.6 | | | |
| $^{38}$Na | 3.199 | 0.491 | 243.4 | | | | | | |
| $^{39}$Na | 3.209 | 0.472 | 244.1 | | | | | | |
| $^{40}$Na | 3.228 | 0.477 | 243.4 | | | | | | |
| $^{24}$Mg | 3.043 | 0.487 | 194.3 | 3.130 | 0.520 | 195.2 | 3.057 | 0.605 | 198.3 |
| $^{25}$Mg | 3.009 | 0.376 | 202.9 | 3.103 | 0.432 | 204.3 | 3.028 | | 205.6 |
| $^{26}$Mg | 2.978 | 0.273 | 212.5 | 3.080 | -0.300 | 213.2 | 3.034 | 0.482 | 216.7 |
| $^{27}$Mg | 3.015 | 0.310 | 220.2 | 3.096 | 0.339 | 221.5 | | | 223.1 |
| $^{28}$Mg | 3.048 | 0.345 | 228.7 | 3.110 | 0.340 | 229.0 | | 0.491 | 231.6 |
| $^{29}$Mg | 3.055 | 0.289 | 234.3 | 3.118 | 0.283 | 235.0 | | | 235.3 |
| $^{30}$Mg | 3.062 | 0.241 | 240.5 | 3.120 | -0.180 | 240.5 | | 0.431 | 241.6 |
| $^{31}$Mg | 3.075 | 0.179 | 245.1 | 3.123 | 0.030 | 246.1 | | | 243.9 |
| $^{32}$Mg | 3.090 | 0.119 | 250.5 | 3.150 | 0.000 | 252.0 | | 0.473 | 249.7 |
| $^{33}$Mg | 3.117 | 0.233 | 253.1 | 3.165 | 0.155 | 253.0 | | | 252.0 |
| $^{34}$Mg | 3.150 | 0.343 | 257.3 | 3.210 | 0.330 | 255.1 | | | 256.7 |
| $^{35}$Mg | 3.173 | 0.388 | 260.5 | 3.239 | 0.393 | 257.8 | | | 257.5 |
| $^{36}$Mg | 3.198 | 0.432 | 263.9 | 3.265 | 0.440 | 260.2 | | | 260.8 |
| $^{37}$Mg | 3.212 | 0.462 | 264.9 | 3.279 | 0.469 | 261.0 | | | |
| $^{38}$Mg | 3.227 | 0.492 | 266.3 | 3.295 | 0.490 | 261.6 | | | |
| $^{39}$Mg | 3.237 | 0.473 | 267.8 | 3.307 | 0.485 | 262.4 | | | |
| $^{40}$Mg | 3.247 | 0.456 | 269.7 | 3.320 | 0.470 | 262.8 | | | |

**Table 5.** Same as Table 4, for Al and Si isotopes.

| Nucleus | RMF | | | SHF | | | Exp. | | |
|---|---|---|---|---|---|---|---|---|---|
| | $r_{ch}$ | $\beta_2$ | BE | $r_{ch}$ | $\beta_2$ | BE | $r_{ch}$ | $\beta_2$ | BE |
| $^{24}$Al | 3.097 | 0.388 | 182.3 | 3.174 | 0.413 | 185.0 | | | 183.6 |
| $^{25}$Al | 3.072 | 0.381 | 197.7 | 3.164 | 0.430 | 199.5 | | | 200.5 |
| $^{26}$Al | 3.052 | -0.275 | 207.8 | 3.122 | 0.315 | 211.4 | | | 211.9 |
| $^{27}$Al | 3.053 | -0.292 | 221.9 | 3.092 | 0.204 | 222.7 | 3.061 | | 225.0 |
| $^{28}$Al | 3.037 | -0.208 | 238.6 | 3.105 | 0.202 | 232.5 | | | 232.7 |
| $^{29}$Al | 3.033 | -0.141 | 245.6 | 3.126 | 0.241 | 241.5 | | | 242.1 |
| $^{30}$Al | 3.070 | -0.184 | 253.8 | 3.139 | 0.194 | 248.7 | | | 247.8 |
| $^{31}$Al | 3.101 | -0.205 | 259.8 | 3.161 | -0.192 | 256.0 | | | 255.0 |
| $^{32}$Al | 3.103 | -0.111 | 261.2 | 3.162 | 0.020 | 262.6 | | | 259.2 |
| $^{33}$Al | 3.165 | -0.333 | 269.4 | 3.183 | 0.000 | 269.8 | | | 264.7 |
| $^{34}$Al | 3.134 | -0.108 | 275.1 | 3.198 | 0.090 | 271.7 | | | 267.3 |
| $^{35}$Al | 3.167 | 0.268 | 274.1 | 3.229 | 0.250 | 274.4 | | | 272.5 |
| $^{36}$Al | 3.173 | -0.189 | 277.7 | 3.254 | 0.320 | 277.4 | | | 274.4 |
| $^{37}$Al | 3.208 | 0.355 | 281.5 | 3.278 | 0.371 | 280.1 | | | 278.6 |
| $^{38}$Al | 3.214 | -0.254 | 283.5 | 3.288 | 0.378 | 281.4 | | | 280.3 |
| $^{39}$Al | 3.236 | -0.299 | 286.7 | 3.383 | -0.121 | 287.1 | | | |
| $^{40}$Al | 3.257 | -0.336 | 290.4 | 3.316 | 0.403 | 284.2 | | | |
| $^{41}$Al | 3.278 | -0.370 | 290.6 | 3.338 | -0.367 | 285.9 | | | |
| $^{42}$Al | 3.281 | -0.355 | 291.2 | 3.341 | -0.339 | 286.2 | | | |
| $^{43}$Al | 3.282 | -0.338 | 292.2 | 3.341 | -0.312 | 286.6 | | | |
| $^{44}$Al | 3.274 | -0.288 | 293.6 | 3.340 | -0.282 | 287.0 | | | |
| $^{45}$Al | 3.271 | -0.263 | 293.5 | 3.338 | -0.250 | 287.6 | | | |
| $^{46}$Al | 3.359 | 0.341 | 294.5 | 3.326 | -0.129 | 287.7 | | | |
| $^{47}$Al | 3.246 | 0.090 | 294.8 | 3.318 | -0.004 | 288.7 | | | |
| $^{48}$Al | 3.319 | -0.252 | 294.0 | 3.347 | -0.060 | 287.6 | | | |
| $^{25}$Si | 3.127 | 0.286 | 185.1 | | | | | | |
| $^{26}$Si | 3.099 | 0.282 | 201.8 | | | | | 0.446 | |
| $^{27}$Si | 3.114 | -0.299 | 216.4 | | | | | | |
| $^{28}$Si | 3.122 | -0.331 | 232.1 | 3.190 | -0.350 | 233.6 | 3.122 | 0.407 | 236.5 |
| $^{29}$Si | 3.035 | 0.001 | 240.7 | 3.176 | -0.272 | 243.1 | 3.118 | | 245.0 |
| $^{30}$Si | 3.070 | 0.148 | 250.6 | 3.170 | -0.210 | 252.6 | 3.134 | 0.315 | 255.6 |
| $^{31}$Si | 3.108 | -0.180 | 259.1 | 3.182 | -0.199 | 261.7 | | | 262.2 |
| $^{32}$Si | 3.137 | -0.201 | 268.5 | 3.200 | -0.200 | 270.5 | | 0.217 | 271.4 |
| $^{33}$Si | 3.131 | -0.084 | 275.6 | 3.196 | 0.010 | 278.1 | | | 275.9 |
| $^{34}$Si | 3.148 | 0.000 | 284.4 | 3.220 | 0.000 | 286.3 | | 0.179 | 283.4 |
| $^{35}$Si | 3.161 | -0.083 | 287.4 | 3.226 | 0.010 | 289.5 | | | 285.9 |
| $^{36}$Si | 3.186 | -0.162 | 291.5 | 3.150 | 0.150 | 292.4 | | 0.259 | 292.0 |
| $^{37}$Si | 3.200 | 0.238 | 295.4 | 3.269 | 0.247 | 295.9 | | | 294.3 |
| $^{38}$Si | 3.218 | 0.281 | 299.8 | 3.290 | 0.310 | 298.2 | | 0.249 | 299.9 |
| $^{39}$Si | 3.224 | 0.263 | 302.4 | 3.298 | 0.292 | 301.4 | | | 301.5 |
| $^{40}$Si | 3.272 | -0.301 | 306.0 | 3.310 | -0.280 | 304.0 | | | 306.5 |
| $^{41}$Si | 3.295 | -0.336 | 310.1 | 3.349 | -0.329 | 307.2 | | | 307.9 |
| $^{42}$Si | 3.318 | -0.369 | 314.6 | 3.330 | -0.350 | 310.0 | | | |
| $^{43}$Si | 3.320 | -0.356 | 315.2 | 3.377 | -0.339 | 311.1 | | | |
| $^{44}$Si | 3.322 | -0.342 | 316.2 | 3.380 | -0.300 | 311.6 | | | |
| $^{45}$Si | 3.316 | -0.308 | 317.5 | 3.374 | -0.282 | 312.9 | | | |
| $^{46}$Si | 3.303 | -0.262 | 319.3 | 3.370 | -0.240 | 313.5 | | | |
| $^{47}$Si | 3.345 | -0.298 | 319.8 | 3.340 | 0.030 | 314.3 | | | |
| $^{48}$Si | 3.263 | 0.001 | 321.8 | 3.350 | 0.000 | 315.4 | | | |

**Table 5.** Same as Table 4, for Al and Si isotopes (continued)

| Nucleus | RMF | | | SHF | | | Exp. | | |
|---|---|---|---|---|---|---|---|---|---|
| | $r_{ch}$ | $\beta_2$ | BE | $r_{ch}$ | $\beta_2$ | BE | $r_{ch}$ | $\beta_2$ | BE |
| $^{49}$Si | 3.290 | 0.045 | 321.1 | | | | | | |
| $^{50}$Si | 3.341 | -0.159 | 321.5 | | | | | | |
| $^{51}$Si | 3.358 | -0.135 | 321.2 | | | | | | |
| $^{52}$Si | 3.371 | 0.082 | 321.4 | | | | | | |
| $^{53}$Si | 3.391 | 0.042 | 321.6 | | | | | | |
| $^{54}$Si | 3.415 | 0.000 | 322.3 | | | | | | |

**Table 6.** Same as Table 4, for P and S isotopes.

| Nucleus | RMF | | | SHF | | | Exp. | | |
|---|---|---|---|---|---|---|---|---|---|
| | $r_{ch}$ | $\beta_2$ | BE | $r_{ch}$ | $\beta_2$ | BE | $r_{ch}$ | $\beta_2$ | BE |
| $^{30}$P | 3.138 | 0.130 | 246.3 | 3.189 | 0.026 | 249.9 | | | 250.6 |
| $^{31}$P | 3.158 | 0.205 | 258.3 | 3.201 | 0.105 | 261.1 | 3.189 | | 262.9 |
| $^{32}$P | 3.174 | -0.143 | 267.1 | 3.216 | 0.069 | 270.9 | | | 270.9 |
| $^{33}$P | 3.201 | -0.183 | 277.5 | 3.246 | -0.167 | 280.5 | | | 281.0 |
| $^{34}$P | 3.201 | -0.082 | 285.8 | 3.248 | 0.001 | 289.9 | | | 287.2 |
| $^{35}$P | 3.216 | -0.001 | 295.4 | 3.265 | 0.000 | 299.2 | | | 295.6 |
| $^{36}$P | 3.227 | 0.120 | 299.5 | 3.272 | 0.007 | 303.3 | | | 299.1 |
| $^{37}$P | 3.246 | 0.209 | 305.0 | 3.290 | 0.148 | 307.4 | | | 305.9 |
| $^{38}$P | 3.260 | 0.250 | 310.4 | 3.313 | 0.240 | 311.7 | | | 309.6 |
| $^{39}$P | 3.275 | 0.288 | 316.1 | 3.334 | 0.301 | 316.1 | | | 315.9 |
| $^{40}$P | 3.281 | 0.274 | 320.1 | 3.343 | 0.290 | 319.6 | | | 319.2 |
| $^{41}$P | 3.288 | 0.261 | 324.4 | 3.355 | 0.295 | 322.7 | | | 324.2 |
| $^{42}$P | 3.306 | 0.301 | 327.3 | 3.371 | 0.320 | 325.6 | | | 326.3 |
| $^{43}$P | 3.346 | -0.323 | 331.7 | 3.398 | -0.320 | 329.0 | | | 330.7 |
| $^{44}$P | 3.346 | -0.302 | 333.3 | 3.398 | -0.293 | 330.6 | | | |
| $^{45}$P | 3.315 | 0.222 | 335.4 | 3.397 | -0.264 | 332.4 | | | |
| $^{46}$P | 3.342 | -0.251 | 337.5 | 3.397 | -0.237 | 334.2 | | | |
| $^{47}$P | 3.341 | -0.232 | 340.0 | 3.399 | -0.218 | 336.0 | | | |
| $^{48}$P | 3.381 | -0.271 | 341.2 | 3.379 | 0.034 | 337.4 | | | |
| $^{49}$ P | 3.328 | 0.088 | 343.2 | 3.387 | 0.012 | 339.3 | | | |
| $^{50}$ P | 3.353 | 0.101 | 343.7 | 3.414 | -0.061 | 339.2 | | | |
| $^{51}$ P | 3.397 | -0.166 | 344.7 | 3.437 | 0.068 | 339.4 | | | |
| $^{52}$ P | 3.403 | 0.109 | 345.2 | 3.462 | 0.079 | 339.7 | | | |
| $^{53}$ P | 3.428 | 0.109 | 346.3 | 3.487 | 0.089 | 340.1 | | | |
| $^{54}$ P | 3.447 | 0.074 | 346.6 | 3.502 | 0.016 | 340.5 | | | |
| $^{55}$ P | 3.468 | 0.037 | 347.4 | 3.525 | 0.001 | 341.2 | | | |
| $^{33}$S | 3.241 | 0.197 | 275.5 | 3.276 | 0.119 | 278.9 | | | 280.4 |
| $^{34}$S | 3.257 | -0.168 | 286.5 | 3.300 | -0.160 | 289.3 | 3.285 | 0.252 | 291.8 |
| $^{35}$S | 3.260 | -0.078 | 295.7 | 3.300 | -0.006 | 299.6 | | | 298.8 |
| $^{36}$S | 3.273 | 0.002 | 306.2 | 3.310 | 0.000 | 309.6 | 3.299 | 0.168 | 308.7 |
| $^{37}$S | 3.285 | 0.152 | 311.6 | 3.319 | -0.008 | 315.1 | | | 313.0 |
| $^{38}$S | 3.300 | 0.228 | 318.6 | 3.340 | 0.210 | 320.2 | | 0.246 | 321.1 |
| $^{39}$S | 3.312 | 0.264 | 325.3 | 3.354 | 0.248 | 326.5 | | | 325.4 |
| $^{40}$S | 3.325 | 0.299 | 332.4 | 3.370 | 0.300 | 332.1 | | 0.284 | 333.2 |
| $^{41}$S | 3.331 | 0.287 | 337.7 | 3.381 | 0.294 | 336.9 | | | 337.4 |
| $^{42}$S | 3.338 | 0.277 | 343.2 | 3.390 | 0.290 | 341.0 | | 0.300 | 344.1 |

**Table 6.** Same as Table 4, for P and S isotopes. (continued)

| Nucleus | RMF | | | SHF | | | Exp. | | |
|---|---|---|---|---|---|---|---|---|---|
| | $r_{ch}$ | $\beta_2$ | BE | $r_{ch}$ | $\beta_2$ | BE | $r_{ch}$ | $\beta_2$ | BE |
| $^{43}$S | 3.359 | 0.318 | 347.2 | 3.413 | 0.326 | 344.7 | | | 346.7 |
| $^{44}$S | 3.381 | 0.367 | 351.0 | 3.440 | 0.370 | 348.3 | | 0.254 | 351.8 |
| $^{45}$S | 3.375 | 0.312 | 353.4 | 3.430 | 0.311 | 350.4 | | | 354.7 |
| $^{46}$S | 3.371 | 0.258 | 356.6 | 3.420 | 0.250 | 352.5 | | | |
| $^{47}$S | 3.385 | 0.257 | 358.5 | 3.428 | -0.214 | 354.8 | | | |
| $^{48}$S | 3.400 | 0.259 | 360.8 | 3.430 | -0.200 | 356.6 | | | |
| $^{49}$S | 3.403 | 0.227 | 362.9 | 3.430 | 0.127 | 358.8 | | | |
| $^{50}$S | 3.403 | 0.189 | 365.5 | 3.440 | 0.120 | 360.8 | | | |
| $^{51}$S | 3.427 | 0.188 | 366.4 | 3.459 | -0.090 | 361.8 | | | |
| $^{52}$S | 3.451 | 0.183 | 367.6 | 3.490 | -0.140 | 362.5 | | | |
| $^{53}$S | 3.463 | 0.158 | 369.1 | 3.508 | -0.113 | 363.6 | | | |
| $^{54}$S | 3.477 | 0.139 | 371.0 | 3.530 | 0.000 | 364.7 | | | |
| $^{55}$S | 3.494 | 0.105 | 371.4 | 3.541 | 0.030 | 365.4 | | | |

## 3.3. Quadrupole deformation

The ground and low-lying excited state deformation systematics for some of the representative nuclei for Ne, Na, Mg, Al, Si, P, and S are analyzed. In Fig. 2, the ground state quadrupole deformation parameter $\beta_2$ is shown as a function of mass number for Ne, Na, Mg, Al, Si, P, and S. The $\beta_2$ value goes on increasing with mass number for Ne, Na, and Mg isotopes near the drip-line. The calculated quadrupole deformation parameter $\beta_2$ for $^{34}$Mg is 0.59 which compares well with the recent experimental measurement of Iwasaki et al [6] ($\beta_2 = 0.58 \pm 0.06$). It was found that this superdeformed state is 3.2 MeV above the ground band. Again, the magnitude of $\beta_2$ for the drip nuclei reduces with neutron number N and again increases. A region of maximum deformation is found for almost all of the nuclei, as shown in the figure. It so happens in cases like Ne, Na, Mg, and Al that the isotopes are maximally deformed, which may be comparable to superdeformed near the drip-line. For Al and Si isotopes, in general, we find oblate solutions in the ground configurations (see Table 5). In many of the cases, the low-lying superdeformed configuration are clearly visible and some of them can be seen in Fig. 2.

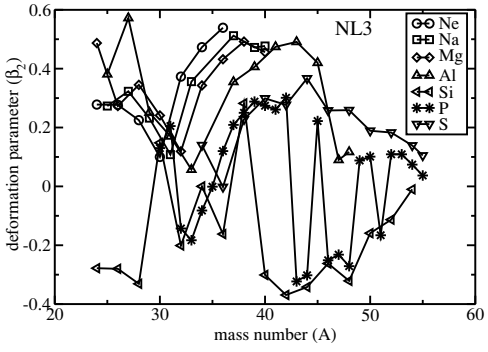


**Figure 2.** The ground state quadrupole deformation parameter $\beta_2$ versus mass number A for Ne, Na, Mg, Al, Si, P, and S isotopes near the drip-line with NL3 parameter set.

## 3.4. Shape coexistence

One of the most interesting phenomena in nuclear structure physics is the shape coexistence [63–66]. In some cases of the nuclei, considered to be near the drip-line, the ground state configuration accompanies a low-lying excited state. In a few cases, it so happens that these two solutions are almost degenerate in energy. For example, in the RMF calculation, the ground state binding energy of $^{24}$Ne is 189.1 MeV with $\beta_2 = -0.259$ and the binding energy of the excited low-lying configuration at $\beta_2 = 0.278$ is 188.9 MeV. The difference in BE of these two solutions is only 0.179 MeV. Similarly the solution of prolate-oblate binding energy difference in SkI4 is 0.186 MeV for $^{30}$Mg with $\beta_2 = -0.183$ and 0.202. These types of degenerate solutions are observed in most of the isotopes near the drip-line. It is worthwhile to mention that in the truncation of the basis space an uncertainty of $\leq 1$ MeV in total binding energy may occur. However, this uncertainty in convergence does not affect determination of the shape co-existence, because both of the solutions are obtained by using the same model space of $N_F = N_B = 12$.

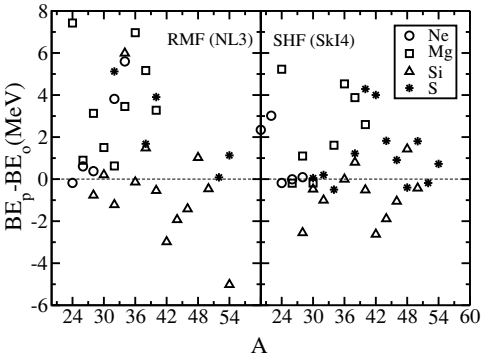


**Figure 3.** The difference in binding energy between the prolate-oblate solutions is shown for even-even Ne, Mg, Si, and S isotopes near the neutron drip-line with NL3 and SkI4 parameter sets.

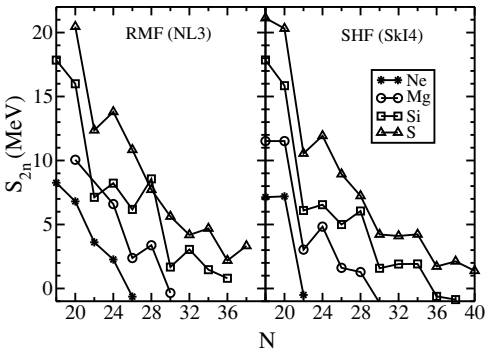


**Figure 4.** The two-neutron separation energy $S_{2n}$ versus neutron number N for neutron-rich Ne, Mg, Si, and S isotopes.

To show this in a quantitative way, we have plotted the prolate-oblate binding energy difference ($BE_p - BE_o$) in Fig. 3. The left hand side of the figure is for relativistic and the right side is for nonrelativistic results. From the figure, it is clear that an island of shape coexistence isotopes are available for Mg and Si isotopes. These shape coexistence solutions are predicted taking into account the intrinsic binding energy. However, the actual quantitative energy difference between ground and excited configurations can be given by performing configuration mixing (mixing such as in the generator coordinate method(GCM) [67]) after the angular momentum projection [64].

## 3.5. Two neutron separation energy ($S_{2n}$)

The appearance of new and the disappearance of known magic numbers near the neutron drip-line is a well-discussed topic currently in nuclear structure physics [9, 68–71]. Some of the calculations in the recent past predicted the disappearance of the known magic number N = 28 for the drip-line isotopes of Mg and S [72–75]. However, magic number 20 retains its magic properties even for the drip-line region. In one of our earlier publications [76], we analyzed the spherical shell gap at N = 28 in $^{44}$S and its neighboring $^{40}$Mg and $^{42}$Si using NL-SH [77] and TM2 parameter sets [57]. The spherical shell gap at N = 28 in $^{44}$S was found to be intact for the TM2 parametrization and is broken for NL-SH. Here, we plot the two-neutron separation energy $S_{2n}$ for Ne, Mg, Si, and S for the even-even nuclei near the drip-line (Fig. 4). The known magic number N = 28 is noticed to be absent in $^{44}$S. On the other hand, the appearance of a sudden decrease in $S_{2n}$ energy at N = 34 in the SHF result is quite prominent, which is not clearly visible in the RMF prediction. This is just two units more than the experimental shell closure at N = 32 [78].

## 3.6. Superdeformation and low Ω parity doublets

The deformation-driving $m = \frac{1}{2}^-$ orbits decrease in energy in superdeformed solutions from the shell above, in contrast to the normal deformed solutions. The occurrence of approximate $\frac{1}{2}^+$, $\frac{1}{2}^-$ parity doublets (degeneracy of $|m|^\pi = \frac{1}{2}^+$, $\frac{1}{2}^-$ states) for the superdeformed solutions are clearly seen in Figs. 5 and 6 where excited superdeformed configurations for $^{32}$Mg, $^{34}$Mg and for $^{46}$Al, $^{47}$Al are given (RMF solutions). For each nucleus, we have compared the normal deformed ($\beta_2 \sim 0.1 - 0.3$) and the superdeformed configurations and analyzed the deformed orbits. The $\frac{1}{2}^+$ and $\frac{1}{2}^-$ states for the single particle levels are shown in Fig. 5 (for $^{32}$Mg and $^{34}$Mg) and Fig. 6 for $^{47}$Al and $^{46}$Al. The occupation of neutron states (denoted by $m^\pi$) in $^{47}$Al and $^{46}$Al is given in Table 7. In both $^{47}$Al and $^{46}$Al two neutrons occupying oblate driving $f_{\frac{7}{2}}$ $m = \frac{7}{2}$ orbits in normal deformation are unoccupied in the superdeformed (SD) case; instead two neutrons occupy the very prolate deformation driving [440]1/2 orbits (raising $n_{\frac{1}{2}^+}$ to 10) which is a superposition of $g_{\frac{9}{2},\frac{7}{2}}$ $d_{\frac{5}{2},\frac{3}{2}}$ $s_{\frac{1}{2}}$ orbits of $N_{osc} = 4$ origin. In $^{46}$Al one $m = \frac{3}{2}^-$ neutron shifts to $m = \frac{1}{2}^-$, enhancing the prolate deformation. It is to be emphasized that the deformations of occupied orbits of self-consistent SD solutions are larger (than their normal deformed counterparts) because of mixing among the shells.

**Table 7.** Occupation of neutron orbits $m^\pi$ in $^{47}$Al and $^{46}$Al driving deformation.

| A | $\beta_2$ | $n_{\frac{1}{2}^+}$ | $n_{\frac{1}{2}^-}$ | $n_{\frac{3}{2}^+}$ | $n_{\frac{3}{2}^-}$ | $n_{\frac{5}{2}^+}$ | $n_{\frac{5}{2}^-}$ | $n_{\frac{7}{2}^+}$ | $n_{\frac{7}{2}^-}$ | $n_{\frac{9}{2}^+}$ |
|---|---|---|---|---|---|---|---|---|---|---|
| $^{47}$Al | 0.09 | 8 | 10 | 4 | 6 | 2 | 2 | 0 | 2 | 0 |
| $^{47}$Al | 0.672 | 10 | 10 | 4 | 6 | 2 | 2 | 0 | 0 | 0 |
| $^{46}$Al | 0.109 | 8 | 9 | 4 | 6 | 2 | 2 | 0 | 2 | 0 |
| $^{46}$Al | 0.701 | 10 | 10 | 4 | 5 | 2 | 2 | 0 | 0 | 0 |

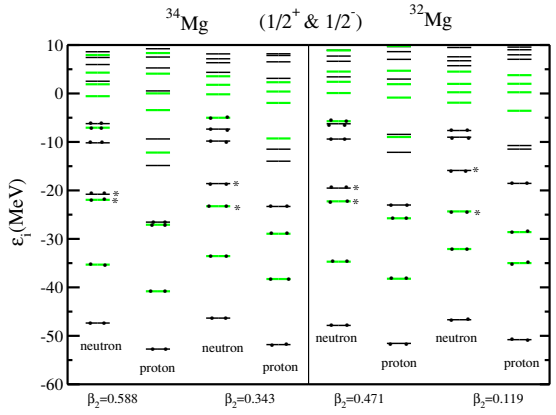


**Figure 5.** The $\frac{1}{2}^+$ and $\frac{1}{2}^-$ intrinsic single-particle states for the normal and superdeformed state for $^{32}$Mg and $^{34}$Mg. Doublets are noticed for the SD intrinsic states only. The $\pm\frac{1}{2}^-$ states are denoted by green lines and the $\pm\frac{1}{2}^+$ states are denoted by black.

### 3.6.1. Structure of superdeformed configuration:

We discus some clear and important characteristics of superdeformed solutions ( $\beta \sim 0.5$ or more) obtained in mean field models as compared to the normal solutions of smaller deformation. Since the lowering and occupation of the deformation-driving $\Omega = \frac{1}{2}$ orbits from the shell above the usual valence space is so important in producing superdeformation, we have emphasized their role in this discussion. There is the occurrence of $\frac{1}{2}^+$, $\frac{1}{2}^-$ orbits close together in energy (doublets) below and near the Fermi surface of the self-consistent superdeformed solutions. This feature also occurs broadly in Nilsson orbits at asymptotically large prolate deformations (see the Nilsson diagrams in Bohr and Mottelson vol. II [79]).

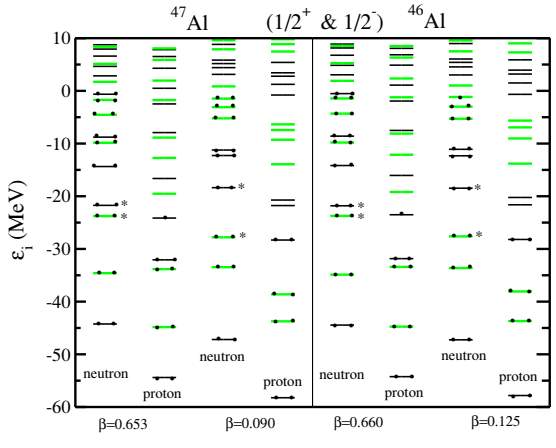


**Figure 6.** The same quantities as in Fig. 5 for $^{46}$Al and $^{47}$Al.

### 3.6.2. Some features of superdeformed solutions:

In normal deformed case, the deformed orbits of a major shell form a "band"-like set of orbits, distinctly separated from the major shell above and below (see Fig. 6 for $^{47}$Al ($\beta$=0.09) and $^{46}$Al ($\beta = 0.125$)). Thus physical states obtained from such intrinsic states of low deformation will be well separated in energy from those intrinsic states where excitation occurs across a major shell (a single nucleon excitation across a major shell means a change in parity and significant energy change for small deformation).

The above mentioned "band"-like separation of orbits of major shells of unique parity is quite lost in the case of superdeformation (see Fig. 6, $\beta$=0.653 of $^{47}$Al and $\beta$=0.660 of $^{46}$Al). The "band"-like orbits now spread in energy (both downward and upward) and orbits of successive major shells come closer to each other in energy; an intermingling of orbits of different parities (see Figs. 5, 6). This is a significant structural change from the case of small deformation. This has also been seen in the case of $^{84}$Zr in a Hartree-Fock study [80, 81].

We would like to emphasize that in the self-consistent models (Skyrme-HF and RMF) the deformation of the nucleus is the result of the deformation of the self-consistently occupied individual orbits:

$$Q = \sum_{i(occupied)} q_i \cdots \tag{13}$$

The occupation of the more deformation-driving orbits from the shell above the valence space and the unoccupation of oblate driving orbits (e.g. $f_{\frac{7}{2}}$, $m = \pm\frac{7}{2}$) contribute much to configuration mixing and the lowering of $m = \frac{1}{2}$ orbits and to generation of the quadrupole deformation. Because of the coming together in energy of $m = \frac{1}{2}^+$ and $\frac{1}{2}^-$ orbits, it is easy to see that superdeformed intrinsic states of two different parities for a particular K quantum number can be formed which will be close to each other in energy. This will lead to parity doublets in band structures. For the neutron-rich nuclei being discussed here, the protons are quite well bound and possible low energy excitations will be those of neutrons near the Fermi surface.

$$|\phi_K >= |\phi^p_{K_p} > |\phi^n_{K_n} > \cdots , \tag{14}$$

where $K_p$ and $K_n$ are the K quantum numbers for proton and neutron configurations (K=$K_p$ + $K_n$).

### 3.6.3. Examples of parity doublet configurations:

We illustrate schematically a possible parity doublet of configurations for neutrons in Fig. 7, the proton configuration $|\phi^p_{K_p}>$ being fixed. We show here the last few neutron occupations of superdeformed solutions and rearrangements near the Fermi surface. In Fig. 7, (b) and (c) are a parity doublet of configurations. $A^+ \rightarrow A^-$ transition between (b) and (c) configurations is of odd parity multipole nature.

Thus, in summary, we find a systematic behaviour of the low Ω (particularly $\frac{1}{2}^+$ and $\frac{1}{2}^-$) prolate deformed orbits for the superdeformed solutions. We notice (from the plot of the orbits) that there is an occurrence of $\frac{1}{2}^+$ and $\frac{1}{2}^-$ orbits very close to each other in energy for the superdeformed (SD) shape. Such $\frac{1}{2}^+$, $\frac{1}{2}^-$ degenerate orbits occur not only for the well-bound orbits but also for the unbound states. For example, the doublet of neutron orbits $[220]\frac{1}{2}^+$ and $[101]\frac{1}{2}^-$ are 4 MeV apart from each other in the normal deformed prolate solutions; but they become degenerate in the superdeformed (SD) solutions (shown by * in Figs. 5 and 6 for Mg, Al). More such doublets are easily identified (Figs. 5 and 6) for superdeformed solutions of $^{32,34}$Mg and $^{46,47}$Al. In fact, it is to be noted that the $\Omega = \frac{1}{2}$ states of unique parity, seen to be clearly well separated in energy from the usual parity orbits in the normal deformed solutions, occur closer to them in energy for the SD states, showing a degenerate parity doublet structure. In fact, for the SD solution the $\frac{1}{2}^+$ and $\frac{1}{2}^-$ orbits are intermixed in the energy plot; while for the normal deformation they occur in distinct groups. This is true both in the Skyrme Hartree-Fock and the RMF calculations.

This can be seen by examining the $\frac{1}{2}^+$ and $\frac{1}{2}^-$ orbits for small and large deformations in Fig. 5. This can lead to parity mixing and octupole deformed shapes for the SD structures [80]. Parity doublets and octupole deformation for superdeformed solutions have been discussed for $^{84}Zr$ [80, 81]. There is much interest for the experimental study of the spectra of neutron-rich nuclei in this mass region [82]. The highly deformed structures for the neutron-rich Ne-Na-Mg-Al nuclei are interesting and signature of such superdeformed configurations (with parity doublet structure) should be looked for.

## 4. Summary and conclusions

In summary, we calculate the ground and low-lying excited state properties, like binding energy and quadrupole deformation $\beta_2$ using RMF(NL3) formalism for Ne, Na, Mg, Si, P, and S isotopes, near the neutron drip-line region. In general, we find large deformed solutions for the neutron-drip nuclei which agree well with the experimental measurement. The calculation is also repeated in the framework of nonrelativistic Hartree-Fock formalism with Skyrme interaction SkI4. Both the relativistic and non-relativistic results are comparable to each other for the considered mass region. In the present calculations a large number of low-lying intrinsic superdeformed excited states are predicted in many of the isotopes and some of them are reported. From the point of view of binding energy, i.e. the sudden fall in $S_{2n}$ value, the breaking of the N = 28 magic number and the likely appearance of a new magic number at N = 34 were noticed in our non-relativistic calculations, in contrast with the RMF findings. This is an indication of more binding than the neighbouring isotopes. However to confirm N = 34 as a magic/non-magic number more calculations are needed. A deformed nucleus has a collective low-lying $2^+$ state. Also, a spherical nucleus can have a fairly low-lying collective $2^+$ state (e.g. Sn nuclei) because of quadrupole collectivity. In this study we find that, for the SD shape, the low Ω orbits (particularly $\Omega = \frac{1}{2}$) become more bound and nearly degenerate with the orbits of opposite parity, i.e. they show a parity doublet structure. Closely lying parity-doublet band structures and enhanced odd parity multipole transitions are possible for the superdeformed shapes.

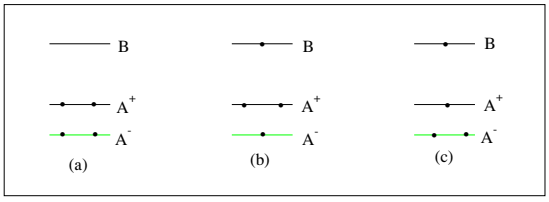


**Figure 7.** With a parity doublet of occupied orbits $A^+$, $A^-$ (having m= ± 1/2 and +ve and -ve parities) and an unoccupied orbit B, possible occupations of neutrons are shown in configurations (a), (b) and (c). The two excited configurations (b) and (c) have the same $K_n$ value and represent two excited bands of different parities (parity doublet). Such situation can occur for neutron configurations in superdeformed $^{47}$Al and $^{32}$Mg, $^{34}$Mg (Figs. 6, 5).

## Acknowledgements

CRP was supported during this work by Project SR/S2/HEP-37/2008 of Department of Science and Technology, Govt. of India.

## References


[1] A. Navin et al., Phys. Rev. Lett. 85, 266 (2000)
[2] H. Iwasaki et al., Phys. Lett. B 491, 8 (2000)
[3] H. Iwasaki et al., Phys. Lett. B 481, 7 (2000)
[4] T. Motobayashi et al., Phys. Lett. B 346, 9 (1995)
[5] K. Tanaka et al., Phys. Rev. Lett. 104, 062701 (2010)
[6] H. Iwasaki et al., Phys. Lett. B 522, 227 (2001)
[7] T. Baumann et al., Nature 449, 1022 (2007)
[8] P. Möller, R. J. Nix, W. D. Myers, W. J. Swiatecki, Atom. Data Nucl. Data 59, 185 (1995)
[9] A. Ozawa, T. Kobayashi, T. Suzuki, K. Yoshida, I. Tanihata, Phys. Rev. Lett. 84, 5493 (2000)
[10] T. Minamisono et al., Phys. Rev. Lett. 69, 2058 (1992)
[11] I. Tanihata, J. Phys. G 22, 157 (1996)
[12] T. Nakamura, J. Phys. Conf. Ser. 312, 082006 (2011)
[13] T. Nakamura et al., Phys. Rev. Lett. 103, 262501 (2009)
[14] D. Vautherin, D. M. Brink, Phys. Rev. C 5, 626 (1972)
[15] P. -G. Reinhard, Rep. Prog. Phys. 52, 439 (1989)
[16] E. Chabanat, P. Bonche, P. Hansel, J. Meyer, R. Schaeffer, Nucl. Phys. A 627, 710 (1997)
[17] M. Bender, Paul-Henri Heenen, P. -G. Reinhard, Rev. Mod. Phys. 75, 121 (2003)
[18] D. Lunney, J. M. Pearson, C. Thibault, Rev. Mod. Phys. 75, 1021 (2003)
[19] J. R. Stone, J. C. Miller, R. Koncewicz, P. D. Stevenson, M. R. Strayer, Phys. Rev. C 68, 034324 (2003)
[20] J. R. Stone, P. -G. Reinhard, Prog. Part. Nucl. Phys. 58, 587 (2007)
[21] J. Erler, P. Klüpfel, P. -G. Reinhard, J. Phys. G: Nucl. Part. Phys. 38, 033101 (2011)
[22] T. Nakatsukasa, Prog. Theor. Exp. Phys. 1, 01A207 (2012)
[23] B. D. Serot, J. D. Walecka, Adv. Nucl. Phys. 16, 1 (1986)
[24] Y. K. Gambhir, P. Ring, A. Thimet, Ann. Phys. (N.Y.) 198, 132 (1990)
[25] D. Vretenar, A. V. Afanasjev, G. A. Lalazissis, P. Ring, Phys. Rep. 409, 101 (2005)
[26] J. Meng et al., Prog. Part. Nucl. Phys. 57, 470 (2006)
[27] T. Nikŝić, D. Vretenar, P. Ring, Prog. Part. Nucl. Phys. 66, 519 (2011)
[28] N. Paar, D. Vretenar, E. Khan, Gianluca Colό, Rep. Prog. Phys. 70, 691 (2007)
[29] P. -G. Reinhard, H. F. Flocard, Nucl. Phys. A 584, 467 (1995)
[30] E. Chabanat, P. Bonche, P. Haensel, J. Meyer, R. Schaeffer, Nucl. Phys. A 635, 231 (1998)
[31] M. A. Preston, R. K. Bhaduri, Structure of Nucleus (Addison-Wesley Publishing Company, Massachusetts, USA, 1975) Ch. 8, 309
[32] S. K. Patra, Phys. Rev. C 48, 1449 (1993)
[33] J. Decharg, D. Gogny, Phys. Rev. C 21, 1568 (1980)
[34] D. G. Madland, J. R. Nix, Nucl. Phys. A 476, 1 (1981)
[35] S. J. Krieger, P. Bonche, H. Flocard, P. Quentin, M. S. Weiss, Nucl. Phys. A 517, 275 (1990)
[36] H. Zhang et al., Eur. Phys. J. A 30, 519 (2006)
[37] S. Raman, C. W. Jr. Nestor, P. Tikkanen, Atom. Data Nucl. Data 78, 1 (2001)
[38] M. Wang et al., Chin. Phys. C 36, 1603 (2012)
[39] I. Angeli, K. P. Marinova, Atom. Data Nucl. Data 99, 69 (2013)
[40] G. Ripka, Adv. Nucl. Phys. 1, 183 (1968)
[41] W. H. Bassichis, B. Giraud, G. Ripka, Phys. Rev. Lett. 15, 980 (1965)
[42] A. Bohr, B. R. Mottelson, Nuclear Structure Vol. I (W. A. Benjamin Inc., New York, 1969)
[43] G. A. Lalazissis, S. Raman, P. Ring, Atom. Data Nucl. Data 71, 1 (1999)
[44] S. K. Patra, M. Del. Estel, M. Centelles, X. Viñas, Phys. Rev. C 63, 024311 (2001)
[45] S. K. Patra, C. R. Praharaj, Phys. Rev. C 44, 2552 (1991)
[46] J. Dobaczewski, H. Flocard, J. Treiner, Nucl. Phys. A 422, 103 (1984)
[47] J. Meng, P. Ring, Phys. Rev. Lett. 77, 3963 (1996)
[48] M. Del Estal, M. Centelles, X. Viñas, S. K. Patra, Phys. Rev. C 63, 044321 (2001)
[49] M. Stoitsov, P. Ring, D. Vretenar, G. A. Lalazissis, Phys. Rev. C 58, 2086 (1998)
[50] H. Nakada, M. Sato, Nucl. Phys. A 699, 511 (2002)
[51] Shan-Gui Zhou, J. Meng, P. Ring, Phys. Rev. C 68, 034323 (2003)
[52] Shan-Gui Zhou, J. Meng, P. Ring, En-Guang Zhao, Phys. Rev. C 82, 011301(R) (2010)
[53] P. Arumugam, B. K. Sharma, S. K. Patra, R. K. Gupta, Phys. Rev. C 71, 064308 (2005)
[54] J. Meng, P. Ring, Phy. Rev. Lett. 77, 3963 (1996)
[55] J. P. Elliott, T. H. R. Skyrme, Proc. R. Soc. London A 232, 561 (1955)
[56] J. W. Negele, Phys. Rev. C 1, 1260 (1970)
[57] Y. Sugahara, H. Toki, Nucl. Phys. A 579, 557 (1994)
[58] G. A. Lalazissis, K. König, P. Ring, Phys. Rev. C 55, 540 (1997)
[59] B. A. Brown, Phys. Rev. C 58, 220 (1998)
[60] R. C. Nayak, L. Satpathy, Atom. Data Nucl. Data 98, 616 (2012)
[61] P. Möller, J. R. Nix, K. -L. Kratz, Atom. Data Nucl. Data 66, 131 (1997)
[62] M. Samyn, S. Goriely, M. Bender, J. M. Pearson, Phys. Rev. C 70, 044309 (2004)
[63] J. P. Maharana, Y. K. Gambhir, J. A. Sheikh, P. Ring,

Phys. Rev. C 46, R1163 (1992)
[64] S. K. Patra, C. R. Praharaj, Phys. Rev. C 47, 2978 (1993)
[65] F. Sarazin et al., Phys. Rev. Lett. 84, 5062 (2000)
[66] J. L. Egido, L. M. Robledo, R. R. Rodriguez-Guzman, Phys. Rev. Lett. 93, 282502 (2004)
[67] N. Onishi, S. Yoshida, Nucl. Phys. 80, 367 (1966)
[68] T. K. Jha, M. S. Mehta, S. K. Patra, B. K. Raj, R. K. Gupta, PRAMANA -J. Phys. 61, 517 (2003)
[69] L. Satpathy, S. K. Patra, Nucl. Phys. A 722, 24c (2003)
[70] R. K. Gupta et al., J. Phys. G 32, 565 (2006)
[71] R. K. Gupta, S. K. Patra, W. Greiner, Mod. Phys. Lett. A 12, 1327 (1997)
[72] T. R. Werner, J. A. Sheikh, W. Nazarewicz, M. R. Strayer, A. S. Umar, M. Misu, Phys. Lett. B 335, 259 (1994)
[73] Ren Zhongzhou, Z. Y. Zhub, Y. H. Cai, Xu Gongou, Phys. Lett. B 380, 241 (1994)
[74] I. Hamamoto, Phys. Rev. C 76, 054319 (2007)
[75] I. Hamamoto, Phys. Rev. C 85, 064329 (2012)
[76] R. K. Gupta, S. K. Patra, W. Greiner, Mod. Phys. Lett. A 12, 1317 (1997)
[77] M. M. Sharma, M. A. Nagarajan, P. Ring, Phys. Lett. B 312, 377 (1993)
[78] R. Kanungo, I. Tanihata, A. Ozawa, Phys. Lett. B 528, 58 (2002)
[79] A. Bohr, B. R. Mottelson, Nuclear Structure, vol. II (W. A. Benjamin Inc., Massachusetts, USA, 1975) Chapter 5
[80] C. R. Praharaj, INT Workshop on Nuclear Many-Body Theories for 21st Century, 24 Sept.- 30 Nov. 2007 (Institute for Nuclear Theory, University of Washington, Seattle, 2007)
[81] C. R. Praharaj, L. Satpathy (Ed.), Structure of Atomic Nuclei (Narosa Publishers, Delhi, 1999) Ch. 4, 108
[82] D. Miller et al., Phys. Rev. C 79, 054306 (2009)